DOI:
10.1038/s41567-019-0487-7

Document Version
Peer reviewed version

Deep-subwavelength features of photonic skyrmions in a confined electromagnetic field with orbital angular momentum

Luping Du[1], Aiping Yang[1], Anatoly V. Zayats[2], Xiaocong Yuan[1]

[1]Nanophotonics Research Centre, Shenzhen Key Laboratory of Micro-Scale Optical Information Technology, Shenzhen University, 518060, China

[2]Department of Physics and London Centre for Nanotechnology, King's College London, Strand, London, WC2R 2LS, United Kingdom

Authors to whom correspondence should be addressed: lpdu@szu.edu.cn, xcyuan@szu.edu.cn, and a.zayats@kcl.ac.uk

In magnetic materials, skyrmions are nanoscale regions where the orientation of electron spin changes in a vortex-type manner[1-4]. Electromagnetic waves carry both spin and orbital angular momenta[5,6]. Here we show that spin-orbit coupling[7-12] in a focused vector beam results in skyrmion-like structure of local photonic spin. While diffraction limits the spatial size of intensity variations, the direction of the electromagnetic field, which defines the polarization and local photonic spin state, is not subject to this limitation. We demonstrate that the local spin direction in the skyrmion-like structure varies on the deep-subwavelength scales down to 1/60 of light wavelength, which corresponds to about 10 nanometre lengthscale. The application of photonic skyrmions may range from high-resolution imaging and precision metrology to quantum technologies and data storage where the local spin state of the field, not its intensity, can be applied to achieve deep-subwavelength optical patterns.

Photonic spin angular momentum (SAM), determined by the light polarization, and orbital angular momentum (OAM) are fundamental characteristics of electromagnetic fields[5,6]. These are considered as two separate degrees of freedom of a paraxial beam[7,8]. However, spin-orbit coupling in focused beams or evanescent waves[9-12] allows for a variety of unusual effects in physics, optics, and metrology[13-17]. Many analogies have recently been developed between electron and optical spin effects, resulting in innovative applications in metrology, sensing, optical information and quantum technologies[3].

One of the prominent manifestation of electron spin-orbit coupling in magnetic materials is the appearance of skyrmions—nanoscale vortexes of electron spins[1-4]. Here we show that spin-orbit coupling in a focused vector beam results in a skyrmion-like photonic spin distribution with the local photon spin vector (i.e., the orientation of the SAM) either along or opposite to orbital angular momentum, depending on the spatial location in a beam cross-section. For waveguided modes featuring evanescent fields, this gives rise to a Neel-type skyrmion structure, while a Bloch-type skyrmion-like SAM configuration is formed within the central area of focused free-space propagating beams. Whereas diffraction phenomenon limits the size of spatial intensity distributions determined by the electromagnetic field amplitude, the direction of the field, which defines its local polarization, is not subjected to this limitation and may vary at much finer, deep-subwavelength scales. We demonstrate that the local spin state of a focused vortex beam varies on the deep-subwavelength scales down to 1/60 of light wavelength, which corresponds to about a lengthscale of 10 nm. We show that such subwavelength spin variations can be readily designed since the presence of a spiral phase in the axial field of the beam carrying orbital angular momentum intrinsically accompanies the spin associated with the transverse field of the beam. The application of the observed photonic skyrmion structures may range from high-resolution imaging and precision metrology to quantum technologies and data storage where the analysis of the local spin structure of the beam, not its intensity, can be applied to achieve deep-subwavelength optical field patterns.

The SAM of the electromagnetic wave can be defined via $\mathbf{S}=\mathrm{Im}(\varepsilon\mathbf{E}^{*}\times\mathbf{E}+\mu\mathbf{H}^{*}\times\mathbf{H})/2\omega$, where **E** and **H** are the electric and magnetic fields, ω is the frequency, and ε and μ are the

permittivity and permeability, respectively.[7] All waveguided and surface electromagnetic waves have an evanescent field component and carry transverse SAM with the spin vector $\boldsymbol{\sigma} = \mathbf{S}/|\mathrm{S}|$ oriented perpendicular to the direction of their propagation[18-21]. Optical vortex beams with helical wavefronts also carry intrinsic OAM described by the vortex topological charge which determines the phase increment around the vortex core[22]. The intensity and local spin vector orientation of the evanescent vortex beam with a topological charge L = +1 is shown in Fig. 1 (see Methods Sections 1 and 2 for the details of the simulations). The spin-orbit coupling in such a beam leads to appearance of a longitudinal SAM (S_z), not present in the evanescent waves without vortices: the oscillations of the electric field vector in a plane perpendicular to the propagation direction (transverse electromagnetic field) can be described by a spin vector parallel to the propagation direction. These longitudinal (S_z) and transverse (S_r) SAMs of the evanescent vortex beam vary across the beam crossection (Fig. 1a,b). A progressive change of the spin vector is seen from the "up" state in the centre to the opposite, "down" state at the position r=r_1 along the radial direction. This structure formed by local photonic spin vectors of the evanescent vortex beam can be proved to be a direct analogue of the structure of the magnetisation direction in the Neel-type skyrmions (skyrmion number n=1, see Methods Section 2) in magnetic materials[23]. It is interesting to note that the free-space propagating nondiffracting vortex vector beams carry the longitudinal and azimuthal SAM components and do not exhibit skyrmion-like spin variations; at the same time, free-space focused propagating vortex beams have a spin vector texture which resembles a Bloch-type skyrmion in the central part of the beam, while the exact analogy does not hold (Methods Section 3).

The energy flux plays an important role in the photonic skyrmion formation (See Methods Section 4). For an evanescent optical vortex (e-OV) with a topological charge L=1, the Poynting vector has only one component along the azimuthal direction due to the presence of OAM in the beam. This is manifested as a series of donut-shaped energy fluxes. The variation of the energy flux density in z-direction induces a r-component of the SAM (S_r), while its variations in r-direction induce a z-component (S_z). The interplay between the two SAM components leads to a distribution of the orientations of local photonic spin vectors which is analogous to the spin texture of a Neel-type magnetic skyrmion. The

multiple azimuthal energy fluxes possess well-defined boundaries (at $r=r_i$, i=1,2,3,…), where the energy flux vanishes $P_\varphi(r_i)=0$. Each domain forms a skyrmion-like feature with a complete spin vector reversal from the "up" to the "down" state (Fig. 2b). The intrinsic spin-momentum locking present in the waveguided modes[7,19] ensures the topological protection in terms of the spin vector direction being completely determined by the mode propagation direction, so that an optical analogy with the quantum spin-Hall effect can be inferred[20]. Therefore, in order to observe the spin vector reversal from the "down" to the "up" state, the propagation direction must be reversed, which can be achieved with L=-1 beam. The spin-momentum locking is preserved even for SPP modes subjected to Ohmic losses in the metal, since the losses influence only intensity of the wave but not spin or propagation direction.

We experimentally demonstrated the spin structure of the evanescent vortex beams on the example of plasmonic vortices.[24,25] We developed a unique scanning near-field optical microscopy set-up which works in a dark-field-like configuration in order to extract a weak Rayleigh scattering signal from the near-field probe (a polystyrene nanoparticle in this work) from the strong background illumination, enabling super-resolved characterisation of the evanescent field polarisation with high signal-to-noise ratio (See Methods Section 5 for the details of the experimental set up). In contrast to the intensity imaging with small metal nanoparticles as a near-field probe,[26-30] dielectric nanoparticles of relatively larger size are needed here to enable super-resolved characterisation of the weak in-plane electric field components (corresponding to the S_z component) of waveguided modes (See Methods Section 6 for the optimisation of the optical response of a dielectric nanosphere). In order to characterize a local longitudinal SAM (S_z), we define a spin-related parameter $\gamma_s=(I_{RCP}-I_{LCP})/(I_{RCP}+I_{LCP})\propto S_z/I$, where I_{RCP} and I_{LCP} are the intensities measured at a given position of the probe of the right- and left-handed circularly polarized components of the transverse field, respectively, and $I= I_{RCP}+I_{LCP}$. Thus, $\gamma_s = +1(-1)$ represents a pure right (left) -handed circular polarization, $\gamma_s=0$ represents a linear polarization, and fractional values represent the elliptical polarizations.

The experimental maps of the local spin structure of the plasmonic vortex beams with angular momenta L = +1, 0 and -1 are presented in Fig. 3. The e-OVs are excited by the

respective vortex beams as shown in the insert. The intensity distributions of RCP and LCP light generated by scattering of the surface plasmon polariton (SPP) vortex beam is in line with the theoretical predictions (Fig. 1 and Supplementary Fig. 5). Both the experiment and simulations show that across the beam cross-section, the local spin vector of the in-plane electric field varies dramatically with the distance to the beam axis. The obtained spin structures for the plasmonic vortices with $L = \pm 1$ reveal the multiple reversals of the spin vector across the vortex, with the spin state in the centre of the beam determined by the net angular momentum of the excitation beam. For a radially polarized incident beam[31] ($L = 0$), the spin structure is not observed, as expected because of the absence of OAM associated with the excited SPPs. For the beams with $L = \pm 1$, the spin vector reversal caused by OAM-SAM coupling is clearly observed with the spin achieving opposite values to the spin of the incident beam, showing efficient OAM to SAM conversion.

In the evanescent vortex beam, the first spin vector reversal is followed by multiple flips of increasing frequency with the increasing distance (Figs. 3 and 4 and Supplementary Fig. 2). Except for the first reversal close to the beam axis for which the distance is on the order of the diffraction limit, the other spin vector reversals take place at the deep-subwavelength scales. For example, the second reversal requires only approximately $\lambda/17$ distance. While the intensity variations within a light beam are subject to the diffraction limit ($\sim \lambda/2$), the spin vector structure which is determined by the direction and not the amplitude of the electric field is not governed by diffraction and can achieve deep-subwavelength resolution. This provides a new concept to modulate optical fields on the deep-subwavelength scales using focused vortex beams which can be used for applications in precision metrology, ultra-sensitive displacement and position sensor, super-resolution imaging, chiral molecule detection, to name but a few. In the above theoretical analysis, the only assumption is a spiral phase associated with the axial field, so the considerations are applicable to any type of vortex beams with this property, being free-space, evanescent or waveguided modes.

The high-resolution cross-sectional profile of the spin state reversal is shown in Fig. 4 for the $L = +1$ beam. It reveals the changes of the spin state from positive to negative on subwavelength scales. Away from the beam centre, the second spin vector reversal (Fig.

4c,d, light green area in Fig. 4a,b) takes place over the distance of 53 nm (37.5 nm from the simulations, Fig. 3c). A more interesting for practical applications is the full-width at half-maximum (FWHM) of the sharp dip between the peaks, which is approximately 15 nm ($\lambda/45$) measured in the experiment (approximately 10 nm or $\lambda/63$ from simulations). The deviation of the experimental observed FWHM from the theoretical predictions is probably due to the relatively large size of the probe nanoparticle. In principle, the use of a nanoparticle with a smaller size could improve the spatial resolution but at the expense of the reduced sensitivity to the in-plane field (Supplementary Fig. S6), which would amplify the inaccuracies in the polarisation determination since the dominant longitudinal field will be recorded in the measurements. It should be noted that much finer structures occur at the higher-order spin vector reversals. Nevertheless, it happens at the expense of the decreased intensity, making them difficult to use in practical applications (see Methods Section 4). The observed sharp features of optical fields, experimentally demonstrated here on the example of SPPs but characteristic for all kinds of waveguided modes and focused vortex beams, can be engineered using spin-orbit coupling in focused vortex beams and serve as a probe for high precision metrology. The approach provides a new concept to modulate optical fields on the deep-subwavelength scales using evanescent vortex beams.

In summary, we showed that an intrinsic connection and transformations between the two forms of angular momenta associated with a confined electromagnetic field allows engineering of local spin state in the focused beam irrespectively of the spin of the incident light. The resultant spin vector variations resemble skyrmions associated with a magnetization orientation in magnetic materials and can be considered as their photonic analogue. It should be mentioned that while this article was in review, an independent work[32] has demonstrated an optical skyrmion lattice formed by interfering multiple SPP waves. This skyrmion lattice was defined in term of the electric field vector variations, which is distinct from our work where the skyrmion structure is described in term of the variations of a local spin direction, which emerge due to the photonic spin-orbit interaction. The topological protection of the skyrmion lattice against the SPP loss was also verified in[32]. The described subwavelength features of the photonic skyrmions can be used for metrology applications, such as sizing of nanoparticles (nanoparticles of different sizes will provide

different degree of broadening of the spin vector reversal dip), a displacement sensor based on the high rate of detectable polarization changes (for the spin vector reversal in Fig. 4d, the sensitivity is estimated to be 2.4 degrees of polarizer rotation per nanometer, which very straightforward measurement allowing to reach sub-nanometer resolution), or nanopositioning (each position within the beam is characterized by a specific polarization). Super-resolution scanning microscopy and chirality mapping, where recording polarisation patterns with a specific local spin could be employed as a virtual probe for circular dichroism, and high-density data storage applications, where circular polarized beams are used to induce local magnetization reversal, may benefit from the deep-subwavelength features of the polarization changes in photonic skyrmion-like fields.

Acknowledgement: This work was supported, in part, by the National Natural Science Foundation of China grants 61622504, 61427819, 61490712 and 11504244, National Key Basic Research Program of China (973) grant 2015CB352004, the leading talents of Guangdong province program grant 00201505, the Natural Science Foundation of Guangdong Province grant 2016A030312010, the Science and Technology Innovation Commission of Shenzhen grants KQTD20150710165601O1, KQTD2017033011044403 and ZDSYS201703031605029, EPSRC (UK) and ERC iCOMM project (789340). A.Z. acknowledges support from the Royal Society and the Wolfson Foundation. L.D. acknowledges the support given by Guangdong Special Support Program. L.D. thanks S. Peng for his assistance with the theoretical analysis.

Author contributions: L.D. and A.Z. developed the concept. L.D. carried out the analytical and numerical modeling. L.D. and X.Y. designed the experiment. A.Y. performed the experiments. L. D., X.Y. and A.V. Z. wrote the manuscript. L.D., X.Y. and A.Z. supervised the work. All the authors discussed the results and commented on the manuscript.

Data availability statement: The data that support the plots within this paper and other findings of this study are available from the corresponding author upon reasonable request.

References:

1 Rossler, U. K., Bogdanov, A. N. & Pfleiderer, C. Spontaneous skyrmion ground states in magnetic metals. Nature **442**, 797-801 (2006).

2 Muhlbauer, S. et al. Skyrmion Lattice in a Chiral Magnet. Science **323**, 915-919 (2009).

3 Yu, X. Z. et al. Real-space observation of a two-dimensional skyrmion crystal. Nature **465**, 901-904 (2010).

4 Heinze, S. et al. Spontaneous atomic-scale magnetic skyrmion lattice in two dimensions. Nat. Phys. **7**, 713-718 (2011).

5 Poynting, J. H. The wave motion of a revolving shaft, and a suggestion as to the angular momentum in a beam of circularly polarised light. Proceedings of the Royal Society of London Series a-Containing Papers of a Mathematical and Physical Character **82**, 560-567 (1909).

6 Allen, L., Beijersbergen, M. W., Spreeuw, R. J. C. & Woerdman, J. P. Orbital angular momentum of light and the transformation of Laguerre-Gaussian laser modes. Physical Review A **45**, 8185-8189 (1992).

7 Bliokh, K. Y., Rodriguez-Fortuno, F. J., Nori, F. & Zayats, A. V. Spin-orbit interactions of light. Nature Photonics **9**, 796-808 (2015).

8 Milione, G., Sztul, H. I., Nolan, D. A. & Alfano, R. R. Higher-Order Poincare Sphere, Stokes Parameters, and the Angular Momentum of Light. Physical Review Letters **107**, 053601 (2011).

9 Zhao, Y., Edgar, J. S., Jeffries, G. D. M., McGloin, D. & Chiu, D. T. Spin-to-orbital angular momentum conversion in a strongly focused optical beam. Physical Review Letters **99**, 073901 (2007).

10 Vuong, L. T., Adam, A. J. L., Brok, J. M., Planken, P. C. M. & Urbach, H. P. Electromagnetic Spin-Orbit Interactions via Scattering of Subwavelength Apertures. Physical Review Letters **104**, 083903 (2010).

11 Bliokh, K. Y. et al. Spin-to-orbital angular momentum conversion in focusing, scattering, and imaging systems. Optics Express **19**, 26132-26149 (2011).

12 Cardano, F., Karimi, E., Marrucci, L., de Lisio, C. & Santamato, E. Generation and dynamics of optical beams with polarization singularities. Optics Express **21**, 8815-8820, (2013).

13 Marrucci, L. Generation of helical modes of light by spin-to-orbital angular momentum conversion in inhomogeneous liquid crystals. Molecular Crystals and Liquid Crystals **488**, 148-162 (2008).

14 Tischler, N. et al. Experimental control of optical helicity in nanophotonics. Light-Science & Applications **3**, e183 (2014).

15 Hao, X., Kuang, C., Wang, T. & Liu, X. Phase encoding for sharper focus of the azimuthally polarized beam. Optics Letters **35**, 3928-3930 (2010).

16 Padgett, M. & Bowman, R. Tweezers with a twist. Nat Photon **5**, 343-348 (2011).

17 Du, L. et al. Broadband chirality-coded meta-aperture for photon-spin resolving. Nature Communications **6**, 10051 (2015).

18 Bliokh, K. Y. & Nori, F. Transverse spin of a surface polariton. Physical Review A **85**, 061801 (2012)

19 Bliokh, K. Y., Bekshaev, A. Y. & Nori, F. Extraordinary momentum and spin in evanescent waves. Nature Communications 5, 3300 (2014)

20 Bliokh, K. Y., Smirnova, D. & Nori, F. Quantum spin Hall effect of light. Science **348**, 1448-1451, (2015)

21 Aiello, A., Banzer, P., Neugebaueru, M. & Leuchs, G. From transverse angular momentum to photonic wheels. Nature Photonics **9**, 789-795 (2015).

22 Padgett, M., Courtial, J. & Allen, L. Light's orbital angular momentum. Physics Today **57**, 35-40 (2004).

23 Kezsmarki, I. et al. Neel-type skyrmion lattice with confined orientation in the polar magnetic semiconductor GaV4S8. Nature Materials **14**, 1116 (2015).

24 Barnes, W. L., Dereux, A. & Ebbesen, T. W. Surface plasmon subwavelength optics. Nature **424**, 824-830 (2003).

25 Kim, H. et al. Synthesis and Dynamic Switching of Surface Plasmon Vortices with Plasmonic Vortex Lens. Nano Letters **10**, 529-536 (2010).

26 Lindfors, K. et al. Local polarization of tightly focused unpolarized light. Nature

Photonics 1, 228-231, (2007).

27 Wang, X.-L. et al. Optical orbital angular momentum from the curl of polarization. Physical Review Letters 105, 253602 (2010).

28 Bauer, T., Orlov, S., Peschel, U., Banzer, P. & Leuchs, G. Nanointerferometric amplitude and phase reconstruction of tightly focused vector beams. Nature Photonics 8, 24-28, (2014).

29 Neugebauer, M., Bauer, T., Aiello, A. & Banzer, P. Measuring the Transverse Spin Density of Light. Physical Review Letters 114, 063901, (2015).

30 Yang, A. P., Du, L. P., Meng, F. F. & Yuan, X. C. Optical transverse spin coupling through a plasmonic nanoparticle for particle-identification and field-mapping. Nanoscale 10, 9286-9291, (2018).

31 Zhan, Q. Cylindrical vector beams: from mathematical concepts to applications. Advances in Optics and Photonics **1**, 1-57 (2009).

32. Tsesses, S., Ostrovsky, E., Cohen, K., Gjonaj, B., Lindner, N. H., Bartal, G. Optical skyrmion lattice in evanescent electromagnetic fields, Science 361, 993–996 (2018).

33. Ishimaru, A., *Electromagnetic wave propagation, radiation, and scattering: From Fundamentals to Applications*. 2nd ed. 2017: Wiley-IEEE Press.

34. Wolf, E., Electromagnetic diffraction in optical systems - I. An integral representation of the image field. Proceedings of the Royal Society of London. Series A. Mathematical and Physical Sciences **253**(1274), 349-357 (1959).

Figures

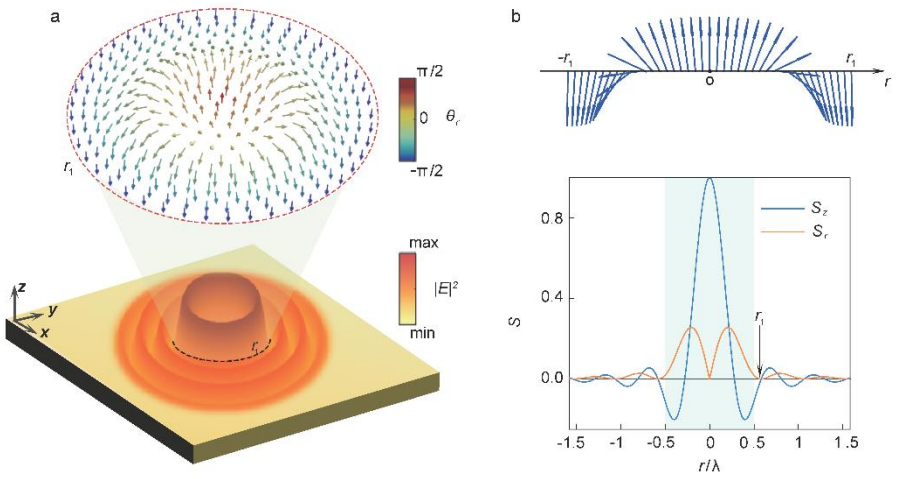

Fig. 1. Spin vector structure of the evanescent field vortex forming the Neel-type photonic skyrmion. (a) Intensity distribution of the evanescent field vortex with a topological charge L=1 (bottom) and the distribution of the photonic spin orientation in the centre of the vortex (top). The arrows indicate the direction of the unit spin vector $\boldsymbol{\sigma}$ determined by θ_r=arctan(S_z/S_r). (b) The radial variations of the transverse (S_r) and longitudinal (S_z) spin components of the beam (bottom) and the orientation of the spin vector in the centre of the beam (top). The in-plane wavevector (k_r) of the evanescent vortex for the above calculation is set to 1.05k_0, where k_0 =2π/λ represents the wavevector in the free space.

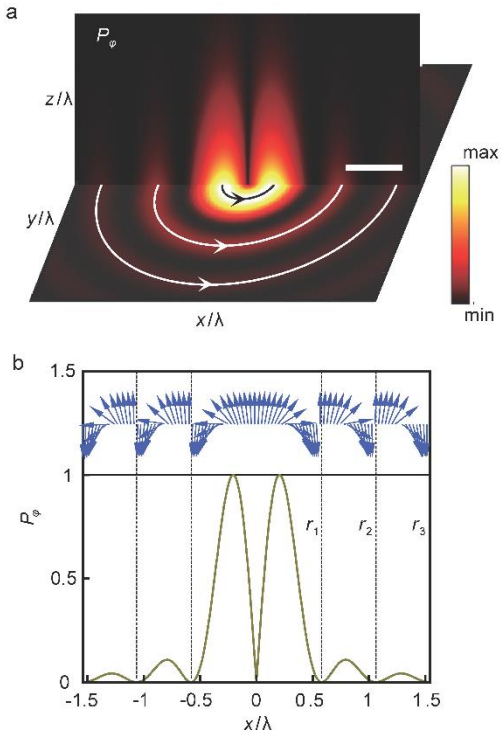

Fig. 2. Energy flux and local spin vector orientation in an evanescent vortex. (a) Energy flux density in the evanescent optical vortex with topological charge L=1. A series of donut-shaped energy fluxes along the azimuthal direction are formed due to the presence of OAM in the beam, resulting in a skyrmion-like structure of local photonic spin vectors in Fig. 1(a). (b) Cross-section of the energy flux density along the radial direction (bottom) and the spin vector variation (top). The domains of spin vector reversal are highlighted with different colors. The scale bar in (a) is $\lambda/2$.

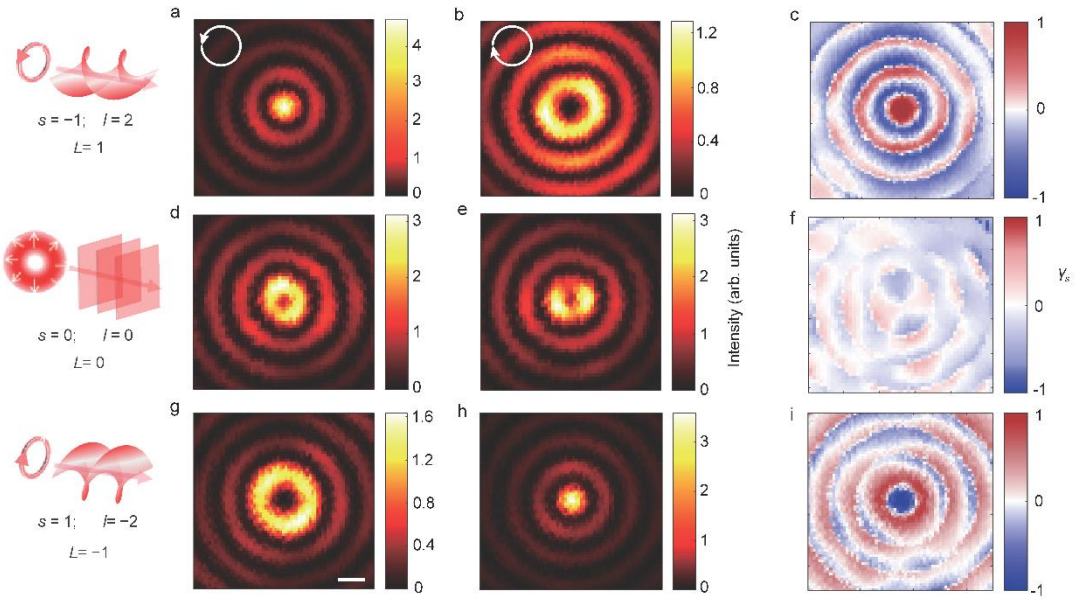

Fig. 3. Local spin structure of a plasmonic vortex. (a-h) The intensity distributions of (a,d,g) RCP and (b,e,h) LCP components of light scattered by a nanoparticle scanning across a plasmonic vortex, and (c,f,i) the corresponding local spin structure of the plasmonic vortex calculated as $\gamma_s=(I_{RCP}-I_{LCP})/(I_{RCP}+I_{LCP})$. Local spin structure of the plasmonic vortices with topological charge of L=+1 (a,b,c), L=0 (d,e,f) and L=-1 (g,h,i) were mapped and multiple spin vector reversals observed for L=±1. The residual spin structure for L=0 in (f) arises mainly from the effect of a linear polarizer present in the experiment. The SPP were excited on a surface of a 50 nm thick Ag film by light with a wavelength of λ = 632.8 nm. A polystyrene nanoparticle of a diameter of 320 nm was used as a scatterer. Scanning step size is 30 nm. All images are of the same size; the scale bar in (g) is $\lambda/2$. The inserts on the left show the structure of the field of the excitation beams with different spin (s) and orbital (l) angular momenta leading to the excitation of plasmonic vortices with $L=s+l$. Simulated maps for the same beam parameters are shown in Supplementary Fig. 5.

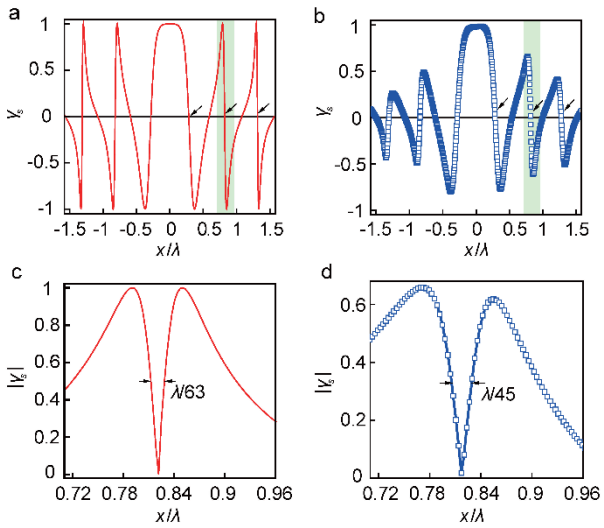

Fig. 4. Deep-subwavelength features in the local photonic spin structure. (a) Simulated and (b) measured traces of the local spin state near the centre of a plasmonic vortex generated with L=+1 beam. Black arrows indicate sub-diffraction variations of the local spin from positive to negative state. (c,d) The detailed view of the spin structure of the areas indicated with green boxes in (a,c), where the local spin reversal takes place on a deep-subwavelength scale. The absolute value of the local spin ($|\gamma_s|$) is shown to facilitate the quantitative characterization of the feature size. In (b,d), a scanning step is 2 nm. All other experimental parameters are as in Fig. 3.

Methods.

1 | Calculations of electromagnetic field in an optical system with axial symmetry.

In order to illustrate the spin-orbit properties in a confined electromagnetic field in an axisymmetric optical system, we consider a propagation of a beam in a source free, homogeneous and isotropic medium for which the Hertz vector potential (Π) can be introduced to reduce the Maxwell's equations to a single scalar differential equation.[33] Assuming exp(-*iωt*) time dependence and propagating in *z*-direction (exp(*ik*$_z$*z*)), the electromagnetic fields of a transverse magnetic (TM) mode in a cylindrical coordinate system (*r, φ, z*) can be described as

$$\begin{aligned}\mathbf{E}&=\left[E_r,\quad E_\varphi,\quad E_z\right]=\left[ik_z\frac{\partial}{\partial r},\quad i\frac{k_z}{r}\frac{\partial}{\partial\varphi},\quad k_r^2\right]\Pi\\ \mathbf{H}&=\left[H_r,\quad H_\varphi,\quad H_z\right]=\left[-\frac{i\omega\varepsilon}{r}\frac{\partial}{\partial\varphi},\quad i\omega\varepsilon\frac{\partial}{\partial r},\quad 0\right]\Pi\end{aligned}\quad , \tag{1}$$

where ε is the permittivity of the medium, ω is the angular frequency of the wave, k_r and k_z are the in-plane and axial wave-vector components, respectively, obeying the relation $k_r^2+k_z^2=k^2=\varepsilon_r k_0^2$, $\varepsilon_r=\varepsilon/\varepsilon_0$ is the relative permittivity of the medium, and k_0 and k are the wavevectors in free space and in the medium, respectively. Similarly, transverse electric (TE mode) can be described as

$$\begin{aligned}\mathbf{H}&=\left[H_r,\quad H_\varphi,\quad H_z\right]=\left[ik_z\frac{\partial}{\partial r},\quad i\frac{k_z}{r}\frac{\partial}{\partial\varphi},\quad k_r^2\right]\Pi\\ \mathbf{E}&=\left[E_r,\quad E_\varphi,\quad E_z\right]=\left[\frac{i\omega\mu}{r}\frac{\partial}{\partial\varphi},\quad -i\omega\mu\frac{\partial}{\partial r},\quad 0\right]\Pi\end{aligned}\quad , \tag{2}$$

where μ=1 is the permeability of the medium. Since both TE and TM modes possess a similar spin property, we only consider TM-modes in the following calculations and analysis.

The Hertz vector potential satisfies the following Hertz wave equation in the cylindrical coordinate system:

$$\frac{1}{r}\frac{\partial}{\partial r}\left(r\frac{\partial\Pi}{\partial r}\right)+\frac{1}{r}\frac{\partial}{\partial\varphi}\left(\frac{1}{r}\frac{\partial\Pi}{\partial\varphi}\right)+k_r^2\Pi=0 \tag{3}$$

with

$$\Pi(r,\varphi,z)=AJ_l(k_r r)\exp(il\varphi)\exp(ik_z z)\ , \tag{4}$$

where A is a complex-valued constant and J_l denotes the Bessel function of the first kind of the order l. This Herz vector potential describes the electromagnetic field with a spiral phase of a topological charge "l".[25] Subsequently, each components of electric and magnetic fields can be obtained using Eqs. (1,2).

2 | Theoretical analysis of photonic spin structure in an evanescent optical vortex.

We first consider the situation for an evanescent optical vortex (e-OV). In this case, the in-plane wave-vector component (k_r) is larger than the wave-vector (k) of the beam, resulting in an imaginary axial wave-vector component (denoted as ik_z). By replacing the z-component wave-vector in Eq. (1) and Eq. (4) with the imaginary value ik_z, we can obtain the electromagnetic fields for a e-OV of a TM-polarised field as

$$\mathbf{E}=\begin{pmatrix}E_r\\E_\varphi\\E_z\end{pmatrix}=\begin{pmatrix}-Ak_zk_rJ_l'(k_rr)\\-Ai\dfrac{lk_z}{r}J_l(k_rr)\\Ak_r^2J_l(k_rr)\end{pmatrix}e^{il\varphi}e^{-k_zz}$$
$$\mathbf{H}=\begin{pmatrix}H_r\\H_\varphi\\H_z\end{pmatrix}=\begin{pmatrix}A\dfrac{\omega\varepsilon l}{r}J_l(k_rr)\\Ai\omega\varepsilon k_rJ_l'(k_rr)\\0\end{pmatrix}e^{il\varphi}e^{-k_zz} \quad . \tag{5}$$

Subsequently, the spin angular momentum (SAM) of the e-OV can be calculated by

$$\mathbf{S}=\frac{1}{2\omega}\mathrm{Im}\left[\varepsilon\mathbf{E}^*\times\mathbf{E}+\mu\mathbf{H}^*\times\mathbf{H}\right] \quad . \tag{6}$$

Substituting Eq. (5) into Eq. (6), one can obtain

$$\mathbf{S}=\begin{pmatrix}S_r\\S_\varphi\\S_z\end{pmatrix}=\begin{pmatrix}A^2\dfrac{\varepsilon k_zk_r^2l}{2\omega r}J_l(k_rr)^2e^{-2k_zz}\\0\\A^2\dfrac{\varepsilon k_r^3l}{2\omega r}J_l'(k_rr)J_l(k_rr)e^{-2k_zz}\end{pmatrix} \quad . \tag{7}$$

With each component of the SAM, we can plot the spin vector structure of the e-OV (Fig. 1 in the main text), which is a photonic analogue of a Neel-type magnetic skyrmion.[23]

On the other hand, the Poynting vector (i.e., the energy flux density) of the e-OV can be calculated by $\mathbf{P}=\mathrm{Re}(\mathbf{E}^*\times\mathbf{H})/2$ and can evaluated to be

$$\mathbf{P}=\begin{pmatrix}P_r\\P_\varphi\\P_z\end{pmatrix}=\begin{pmatrix}0\\\frac{1}{2}A^2k_r^2\frac{\omega\varepsilon l}{r}J_l\left(k_r r\right)^2e^{-2k_z z}\\0\end{pmatrix}\quad . \tag{8}$$

By analyzing the expressions for the SAM and the Poynting vector, we can see that the SAM is related to the energy flux density via

$$\mathbf{S}=\frac{1}{2\omega^2}\nabla\times\mathbf{P}=\frac{1}{2\omega^2}\left(-\frac{\partial P_\varphi}{\partial z}\hat{r}+\frac{1}{r}\frac{\partial\left(rP_\varphi\right)}{\partial r}\hat{z}\right)\quad . \tag{9}$$

In order to further verify the skyrmion analogy, we calculate the skyrmion number (n) of the spin vector structure[4]

$$n=\frac{1}{4\pi}\iint\mathbf{M}\cdot\left(\frac{\partial\mathbf{M}}{\partial x}\times\frac{\partial\mathbf{M}}{\partial y}\right)dxdy\,, \tag{10}$$

where **M** stands for the unit vector in the direction of the local SAM vector within the e-OV, and the integral is taken over a unit cell of skyrmion in the horizontal plane. Since the SAM contains only the r- and z-component, **M** can be represented as

$$\mathbf{M}=\begin{pmatrix}M_r\\M_\varphi\\M_z\end{pmatrix}=\begin{pmatrix}\cos\theta_r\\0\\\sin\theta_r\end{pmatrix}\quad , \tag{11}$$

where θ_r is the orientation angle of the SAM vector with respect to the X-Y plane, and independent of the azimuthal angle φ. Thus, Eq. (10) results in

$$n=\frac{1}{2}\int_{r_i}^{r_{i+1}}\cos\theta_r\frac{\partial\theta_r}{\partial r}dr\quad .$$

where r_i (i=1,2,3,…) denote the positions where the energy flux density vanishes ($P_\varphi(r_i)$=0). For a photonic spin structure with the spin vector changing progressively from the "up" state to the "down" state at each domain defined by ($r\in[r_i, r_{i+1}]$, $\varphi\in[0, 2\pi]$) as shown in Fig. 2, Eq. (10) can be evaluated as n = 1. Thus, the skyrmion number of an e-OV has an integer value of "1" or "-1", with the sign depending on the chiral property (positive or negative spin is observed at r=0) of e-OV. The skyrmion number is determined by the topological property of an electromagnetic field. The azimuthal energy fluxes which induce the SAM in an e-OV possess a donut-shaped profile with a genus 1.

3 | Theoretical analysis of photonic spin structure in a propagating vortex beam.

In the case of a propagating beam with an in-plane wave-vector $k_r<k$, the electric and magnetic fields of a TM-mode can be calculated by substituting Eq. (4) into Eq. (1):

$$\mathbf{E}(k_r)=\begin{pmatrix}E_r\\E_\varphi\\E_z\end{pmatrix}=\begin{pmatrix}iAk_zk_rJ_l'(k_rr)\\-A\dfrac{lk_z}{r}J_l(k_rr)\\Ak_r^2J_l(k_rr)\end{pmatrix}e^{il\varphi}e^{ik_zz}$$
$$\mathbf{H}(k_r)=\begin{pmatrix}H_r\\H_\varphi\\H_z\end{pmatrix}=\begin{pmatrix}A\dfrac{\omega\varepsilon l}{r}J_l(k_rr)\\Ai\omega\varepsilon k_rJ_l'(k_rr)\\0\end{pmatrix}e^{il\varphi}e^{ik_zz} \quad . \tag{12}$$

This describes an ideal diffraction-free Bessel vortex beam propagating in z-direction. Subsequently, the SAM can be calculated using Eq. (6) as

$$\mathbf{S}=\begin{pmatrix}S_r\\S_\varphi\\S_z\end{pmatrix}=\begin{pmatrix}0\\A^2\dfrac{\varepsilon k_zk_r^3}{2\omega}J_l'(k_rr)J_l(k_rr)\\A^2\dfrac{\varepsilon k_rl}{2\omega r}\left(k_z^2+\varepsilon_rk_0^2\right)J_l'(k_rr)J_l(k_rr)\end{pmatrix} \tag{13}$$

As can be seen, in contrast to an e-OV for which the SAM contains only the r- and z-components and forms a Neel-type skyrmion structure, the SAM of a propagating Bessel vortex beam contains only the φ- and z-components (Supplementary Fig. 1 (a)) which is characteristic for a Bloch-type skyrmion. The orientation angle (θ_φ) of the SAM vector with respect to the X-Y plane obtained from

$$\tan\theta_\varphi=\frac{S_z}{S_\varphi} \tag{14}$$

is plotted in Supplementary Fig. 1 (b) together with the SAM vector distribution in the x-direction (Supplementary Fig. 1 (c)). As can be seen, although the SAM vector changes progressively towards the azimuthal direction at the central area, there is an abrupt change of SAM at the positions where $S_\varphi=0$, and the SAM vector will never become anti-parallel to the central one, so that skyrmion is not formed. The reason is that a diffraction-free propagating beam is boundary-free in the propagation direction, thus unable to form a well-

defined topology structure. This is in contrast to an e-OV with the intensity decaying exponentially in *z*-direction because of the evanescent nature of the field.

However, in a focused vortex beam (FVB), this abrupt change of SAM can be overcome, enabling us to achieve a skyrmion-like photonic spin structure of a Bloch type in the central area at the focal plane. In a FVB, the diffracted field near focal plane can be evaluated using the Debye approximation, with a rigorous theory developed by Richards and Wolf.[34] To achieve a TM-mode near focal plane, a radially-polarized optical vortex (topological charge *l*) is used as incident beam. After focusing, the electromagnetic field near focal plane can be calculated with the Richards-Wolf theory as

$$\mathbf{E}=\begin{pmatrix}E_r\\E_\varphi\\E_z\end{pmatrix}=\begin{pmatrix}\int_0^{\theta_{\max}}\mathrm{A}(\theta)\left\{ik_z J_l'(k_r r)e^{il\varphi}\right\}e^{ik_z z}d\theta\\ \int_0^{\theta_{\max}}\mathrm{A}(\theta)\left\{-\frac{lk_z}{k_r r}J_l(k_r r)e^{il\varphi}\right\}e^{ik_z z}d\theta\\ \int_0^{\theta_{\max}}\mathrm{A}(\theta)\left\{k_r J_l(k_r r)e^{il\varphi}\right\}e^{ik_z z}d\theta\end{pmatrix}=\int_0^{\theta_{\max}}\mathrm{A}(\theta)\frac{1}{k_r}\mathbf{E}(k_r)d\theta$$

$$\mathbf{H}=\begin{pmatrix}H_r\\H_\varphi\\H_z\end{pmatrix}=\begin{pmatrix}\int_0^{\theta_{\max}}\mathrm{A}(\theta)\left\{\frac{\omega\varepsilon l}{k_r r}J_l(k_r r)e^{il\varphi}\right\}e^{ik_z z}d\theta\\ \int_0^{\theta_{\max}}\mathrm{A}(\theta)\left\{i\omega\varepsilon J_l'(k_r r)e^{il\varphi}\right\}e^{ik_z z}d\theta\\ 0\end{pmatrix}=\int_0^{\theta_{\max}}\mathrm{A}(\theta)\frac{1}{k_r}\mathbf{H}(k_r)d\theta \qquad (15)$$

with

$$\mathrm{A}(\theta)=i^{m+1}A_r t^p(\theta)\, f e^{-ikf} l_0(\theta)\sqrt{\frac{n_0}{n_1}\cos\theta}\sin\theta \quad , \qquad (16)$$

where f is the focal length, $t^p(\theta)$ is the transmission coefficient of the multilayer structure located at the focal plane for a *p*-polarized light, $l_0(\theta)$ is the amplitude profile of incident beam, $\theta_{\max}$ is the maximum incident angle allowed by the focusing lens which is determined by the numerical aperture (NA) as NA= $n_0 \cdot \sin(\theta_{\max})$, n_0 and n_1 are the refractive indices of media in the incident and output space, respectively. The in-plane wave-vector (k_r) is related to the incident angle (θ) by $k_r = n_0 k_0 \sin\theta$. As the result, the electromagnetic field near a focal plane is the superposition of the diffraction-free Bessel vortex beams with different in-plane wave-vectors (Eq. (15)).

After obtaining the electromagnetic field, the SAM of a FVB near a focal plane

(Supplementary Fig. 1 (d)) can be calculated using Eq. (6). Comparing the SAM distribution and the orientation angle of the SAM vector for ideal and focused vortex beams (cf Supplementary Fig. 1 (a-c) and Supplementary Fig. 1 (d-f)), we can find a remarkable difference. The S_z and S_φ SAM components do not intersect at the zero point for a FVB as they do for a nondiffracting vortex beam, and there exists a spin state at $r=r_0$ where $S_\varphi=0$ and the SAM vector ($|\mathbf{S}| = S_z$) is anti-parallel to one at the centre: the spin vectors which point to the $+z$ direction at the geometric centre, change progressively towards the azimuthal direction, and eventually to the opposite $-z$ direction at $r=r_1$. As the result, a Bloch-type skyrmion-like photonic spin structure is formed within the central circular area that is defined by r_1 [23]. Nevertheless, it must be pointed out that outside this area, the spin vector does not exhibit a regular change from the positive to the negative state any more. Therefore, it cannot be treated as a rigorous analogue of a Bloch-type skyrmion.

4 | The relationship between S_z and γ_s.

In order to understand the underlying physics behind formation of the subwavelength features in the spin vector orientation, we plot the spatial variations of the longitudinal SAM ($|S_z|$), the intensity of transversal field (I_{xy}) and the spin parameter ($|\gamma_s|$) in Supplementary Fig. 2. Since the above three parameters have a simple relationship: $\gamma_s \propto S_z/I_{xy}$, we can infer that the spin parameter ($|\gamma_s|$) reaches its maxima of 1 (corresponding to the right-handed or left-handed circular polarization) at the points where the two curves of $|S_z|$ and I_{xy} are tangent, as highlighted with green dashed lines in Supplementary Fig. 2, and the deep-subwavelength features occur between the two peaks.

It should be noted that the subwavelength features of the spin vector reversal occur near the locations of minima of the amplitude, and a finer structure of the spin vector distribution is at the expense of the intensity of the field. Indeed, several spin vector reversals are observed on the decreasing lengthscales with the distance from the center of the beam: $\lambda/16$, $\lambda/63$ (discussed in the main text) and $\lambda/103$ in the plotted range of distances (Supplementary Fig. 2). However, the associated intensity decreases with the decreasing feature size, so that higher-order spin vector reversals become impractical for applications. We have chosen the 2nd feature with $\lambda/63$ size to focus on in this work, as it has a deep-

subwavelength size and sufficient associated light intensities, easily observable in the experiment, therefore, suitable for potential for practical applications.

5 | Experimental setup for characterizing the spin structure in a surface plasmon vortex.

The experimental setup for studies of the super-fine spin structure of a tightly-focused surface plasmon polariton (TM-type evanescent wave) on a metal-air interface is shown in Supplementary Fig. 3. An incident laser beam (a wavelength of 632.8 nm) is tightly focused using an oil-immersion objective lens (Olympus, 100×, NA=1.49) onto the sample consisting of a 3-layer structure of a 50 nm thick silver film on a silica substrate with air as a superstrate. This provides an excitation of SPPs on an air-silver interface. A polystyrene (PS) nanoparticle of a diameter of 320 nm is immobilized onto the silver surface using 4-MBA molecular linkers in order to scatter the SPP in a far-field. The scattered light which contains the local spin information is collected by another objective lens (Olympus, 60×, NA=0.7) and sent through a beam splitter to 2 polarization analysing systems each composed of a combination of $\lambda/4$ waveplate and linear polarizer. One set is arranged at an angle of 45^{o} between the waveplate and the polarizer to detect only RCP light and the other set at an angle of -45^{o} to detect the LCP light. After polarization selection, the intensity of light of each CP components is measured with photomultipliers (PMT). The sample is fixed onto a piezo-scanning stage (resolution of 1 nm) for mapping the local spin structure by scanning the nanoparticle across the beam profile.

A typical back focal image of the reflected beam from the 3-layer structure is captured with CCD1 and is shown in Supplementary Fig. 4 (a), where a dark ring indicates the excitation of the SPPs at the air-silver interface. In order to spatially separate a weak SPP scattering from a nanoparticle and a directly transmitted background light, a circular opaque mask is inserted into the beam path and an annular beam is formed to illuminate a sample via the focusing objective lens. The size of the mask is carefully designed in order not to affect the excitation of the SPPs while to block incident light at low incident angles (Supplementary Fig. 4 (b)). The annular beam is over-focused slightly onto the sample such

that the SPP scattering from a nanoparticle is collected and focused at a point different from the transmitted annular beam along the optical axis. The Rayleigh scattering image of a single PS nanosphere captured at CCD2 is shown in Supplementary Fig. 4 (c), from which we can clearly observe the spatial separation of the Raleigh scattering signal from the particle and the transmitted light. As a result, by placing a fiber coupler (which acts as a pinhole) near the imaging plane of the collection objective lens, the scattered light can be separated from the background direct transmission. Supplementary Fig. 4 (d) shows a dark field image of the PS nanoparticles immobilized on the silver film, demonstrating well separated particles allowing for single-nanoparticle studies.

6 | Investigation of the optical response of a polystyrene nanosphere.

In this work, polystyrene nanosphere with diameter of 320 nm is employed as the near-field scatter in order to out-couple the SPP field with a certain local spin state into the far-field scattering radiation of elliptical polarization. In order to understand the optical response of the PS nanosphere, we performed numerical simulation with finite-difference time-domain method by using the commercial software Lumerical.

The schematic diagram of the structure is shown in Supplementary Fig. 6 (a). In the simulation, the silver film thickness is set to 50 nm. The refractive indices of air, glass substrate and PS nanosphere are set to 1, 1.51 and 1.48, respectively, and that for the silver film is obtained from the Material Database in the software. The gap between the nanosphere and silver film is set to 2 nm, to mimic the separation that created by the 4-MBA molecules, which is employed in the experiment to facilitate the formation of isolated PS nanospheres on the silver film. In the simulation set-up, the incident beam at 633 nm with total field scattered field (TFSF) scheme is employed.

Supplementary Fig. S6 (b-c) show the calculated far-field scattering radiation patterns from the PS nanosphere at the Fourier domain, under the illumination with an *x*-polarized and a *z*-polarized incident light, respectively. As can be seen, a transversal electric field excites a scattering radiation mainly concentrated at small angles, while a longitudinal electric field primarily at larger angles. Considering the NA of the collection objective lens

that is used in the experiment (NA=0.7), the collection efficiency ratio is plotted in Supplementary Fig. 6 (d) for various nanosphere sizes. The plot shows that the PS nanosphere is more sensitive to the transverse electric field component of the evanescent wave than to the longitudinal one. Their collection efficiency ratio is optimized for a diameter of approximately 300 nm for NA = 0.7, showing more than 2 orders of magnitude rejection. This ensures that our set-up characterizes the spin property that is associated with the transverse field of SPP, despite a strongly dominant longitudinal electric field in SPP wave (typically, the intensity of longitudinal field is one order of magnitude higher than the transverse one in the visible spectral range).

Finally, we would like to point out that despite small metal nanoparticles provide higher spatial resolution as near-field probes in intensity imaging, they can hardly be applied for the polarization imaging. A plasmonic gap mode formed by a nanoparticle placed near the interface is more sensitive to the longitudinal field rather than the transverse one. For this reason, metal nanoparticles are typically employed for mapping the longitudinal component of an evanescent field,[30] which alone cannot reveal spin information of an electromagnetic field. Therefore, the use of larger dielectric nanoparticles is advantageous, for which size can be optimized for spin-sensitive measurements (Supplementary Fig. 6 (d)).

Supplementary Information

Deep-subwavelength features of photonic skyrmions in a confined electromagnetic field with orbital angular momentum

Luping Du[1], Aiping Yang[1], Anatoly V. Zayats[2], Xiaocong Yuan[1]

[1]Nanophotonics Research Centre, Shenzhen Key Laboratory of Micro-Scale Optical Information Technology, Shenzhen University, 518060, China

[2]Department of Physics and London Centre for Nanotechnology, King's College London, Strand, London, WC2R 2LS, United Kingdom

Authors to whom correspondence should be addressed: lpdu@szu.edu.cn, xcyuan@szu.edu.cn, and a.zayats@kcl.ac.uk

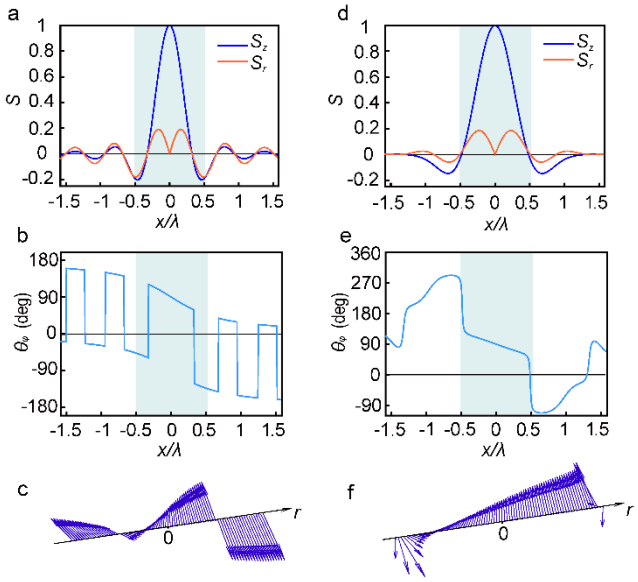

Supplementary Figure 1 | Bloch-type skyrmion-like photonic spin vector structure in a focused vortex beam. (a) The normalized SAM of an ideal diffraction-free Bessel vortex beam of topological charge l=1 with k_r=0.9k_0 containing only φ- and z-components. (b) The orientation angle of the SAM vector with respect to the x-y plane and (c) the SAM vector distribution along the radial direction (within the light green region in (b)) calculated from the data in (a). (d-f) The same as in (a-c) for a focused vortex beam of topological charge l=1 obtained by focusing a radially-polarized beam using numerical aperture NA=0.9. The resultant beam is a superposition of the beams in (a) with different k_r wavevectors (0 – 0.9k_0) determined by NA.

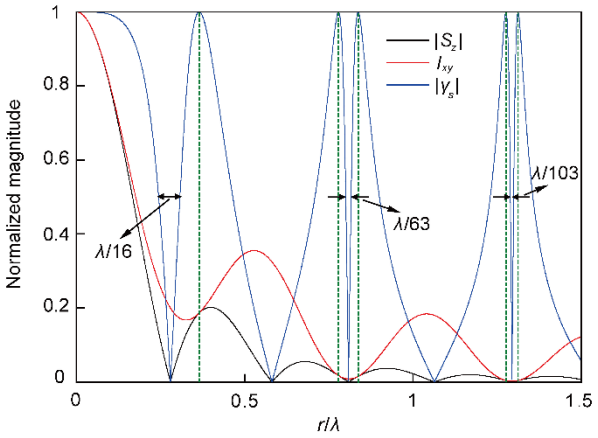

Supplementary Figure 2 | The plots of the radial variations of the longitudinal SAM ($|S_z|$), the intensity of transverse field (I_{xy}) and the spin parameter ($|\gamma_s|$). The curves for $|S_z|$ and I_{xy} are normalized for clear comparison. The dashed green lines indicate the states with pure circular polarization.

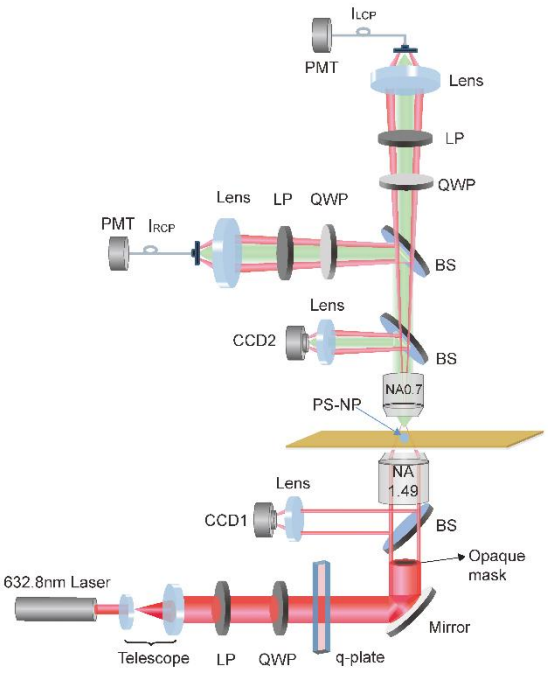

Supplementary Figure 3 | Experimental setup for characterization of the spin structure in a SPP vortex. LP: linear polarizer; HWP: half wave plate; QWP: quarter wave plate; BS: beam splitter; q-plate: a liquid crystal birefringent plate with unit topological charge for vortex beam generation; PMT: photo-multiplier tube; CCD: charge-coupled device.

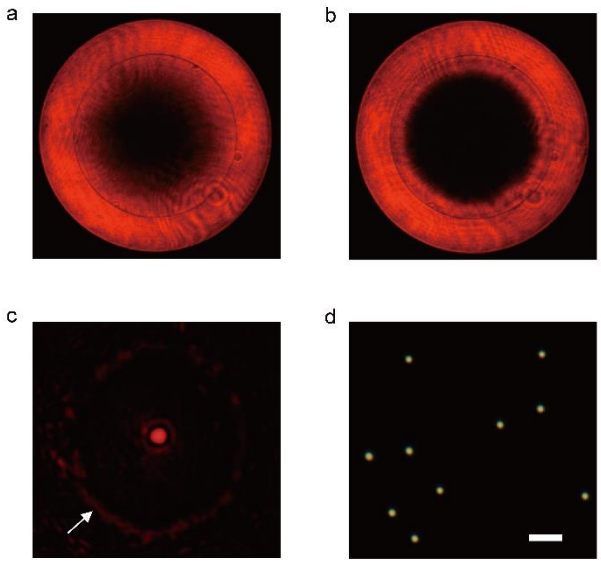

Supplementary Figure 4 | (a) Back focal plane image of the reflected beam from the oil-immersion objective lens, where a narrow dark ring indicates the excitation of SPP at the air-silver interface. (b) The same image when a circular opaque mask is inserted into the beam path, which blocks incident light at low angles while does not affect the excitation of the SPPs. (c) Rayleigh scattering image of a PS nanoparticle captured with CCD2 from the transmission side, clearly illustrating the spatial separation of the scattering signal from the PS nanosphere (central bright spot) and the directly transmitted light (the outside ring profile marked with a white arrow. (d) Dark-field image of the isolated PS nanospheres immobilized on the silver film. The scale bar in (d) is 5 μm.

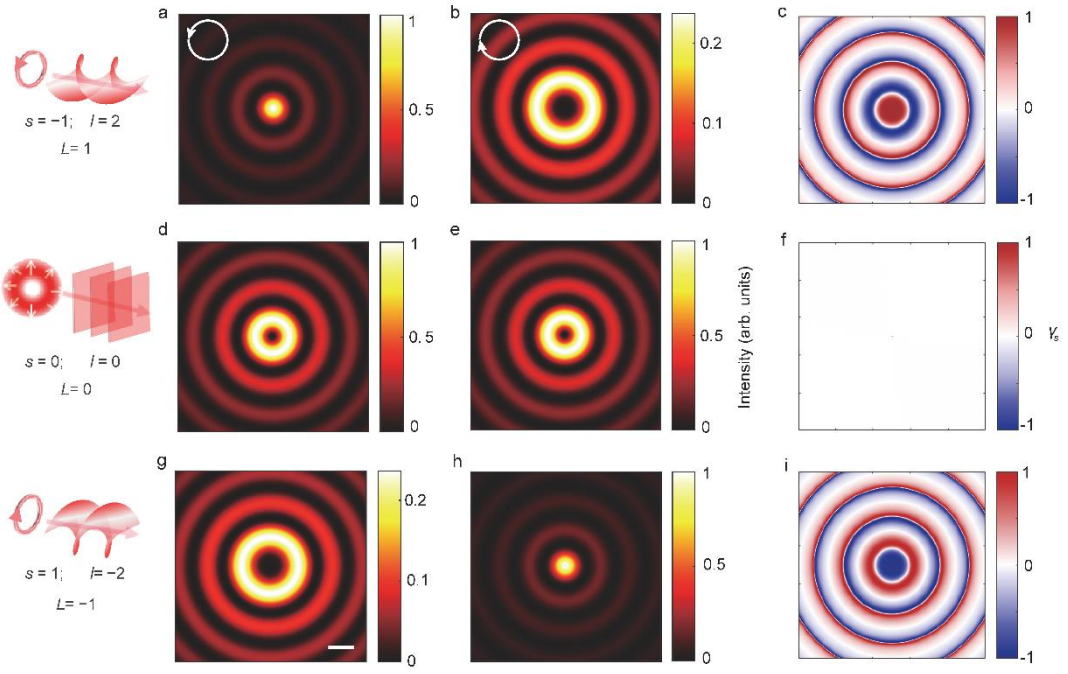

Supplementary Figure 5 | Simulated local spin structure of the plasmonic vortex for $k_r = k_{spp} = 1.05k_0$ to be compared with the experimental results in Fig. 3 in the main text. All images are of the same size; the scale bar in (g) is $\lambda/2$.

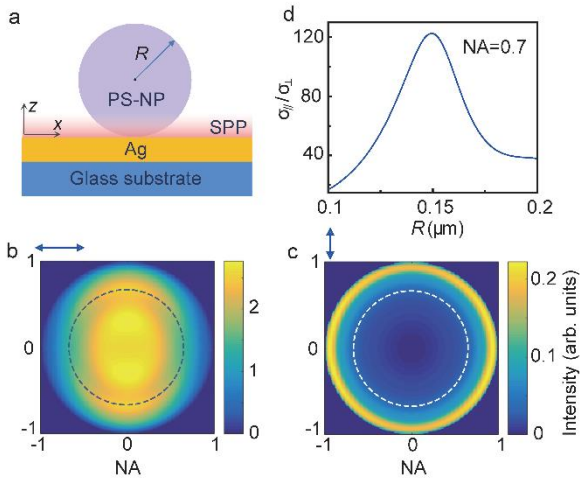

Supplementary Figure 6 | Investigation of the optical response of a PS nanosphere. (a) Schematic diagram of the structure investigated in the simulation. (b-c) The calculated far-field scattering radiation patterns from the PS nanosphere in the Fourier domain, under the illumination with an *x*-polarized and a *z*-polarized incident light, respectively. The dashed circle represents the NA of the collection system employed in the experiment. (d) The ratio of the collection efficiencies of the scattering of the transverse and longitudinal electric fields for NA=0.7.